

Photonic Simulation of Entanglement Growth After a Spin Chain Quench

Ioannis Pitsios,^{1,2} Leonardo Banchi,³ Adil S. Rab,⁴ Marco Bentivegna,⁴ Debora Caprara,⁴ Andrea Crespi,^{1,2} Nicolò Spagnolo,⁴ Sougato Bose,^{3,*} Paolo Mataloni,⁴ Roberto Osellame,^{1,2,†} and Fabio Sciarrino^{4,‡}

¹*Istituto di Fotonica e Nanotecnologie - Consiglio Nazionale delle Ricerche (IFN-CNR),*

P.za Leonardo da Vinci, 32, I-20133 Milano, Italy

²*Dipartimento di Fisica - Politecnico di Milano,*

P.za Leonardo da Vinci, 32, I-20133 Milano, Italy

³*Department of Physics and Astronomy, University College London,
Gower Street, WC1E 6BT London, United Kingdom*

⁴*Dipartimento di Fisica - Sapienza Università di Roma, P.le Aldo Moro 5, I-00185 Roma, Italy*

The time evolution of quantum many-body systems is one of the least understood frontiers of physics. The most curious feature of such dynamics is, generically, the growth of quantum entanglement with time to an amount proportional to the system size (volume law) even when the interactions are local. This phenomenon, unobserved to date, has great ramifications for fundamental issues such as thermalisation and black-hole formation, while its optimisation clearly has an impact on technology (e.g., for on-chip quantum networking). Here we use an integrated photonic chip to simulate the dynamics of a spin chain, a canonical many-body system. A digital approach is used to engineer the evolution so as to maximise the generation of entanglement. The resulting volume law growth of entanglement is certified by constructing a second chip, which simultaneously measures the entanglement between multiple distant pairs of simulated spins. This is the first experimental verification of the volume law and opens up the use of photonic circuits as a unique tool for the optimisation of quantum devices.

The universal features of quantum many-body dynamics remain poorly understood sparing the glimpses provided by a small set of solvable models¹. This is largely because a classical computer fails to keep track of the extensive growth of quantum entanglement in typical cases. One way for enhancing our understanding of such dynamics is to mimic it with another, more controllable “quantum” system – a quantum simulator, as suggested by Feynman². It is then imperative that a true quantum simulator platform, which eventually aims to outperform classical computers, should be able to capture the extensive growth of entanglement in a many-body simulation. For example, a sudden global change of a many-body Hamiltonian (a quantum quench) can induce a dynamics that ultimately entangles two complementary parts of the system by an amount proportional to their size (a volume law)^{3–6}. This quench induced entanglement growth is a phenomenon of pivotal importance, as it not only underpins the ubiquitous process of thermalisation^{4,7}, but, through a holographic correspondence, the dynamical formation of black holes in space-time^{8,9}. Despite the recent remarkable measurements of entanglement¹⁰ and its “propagation”^{11–13} due to quenches in atomic/ionic many-body simulators, the key feature of entanglement growth in proportion to system size remains unverified. Although this verification, for fundamental reasons, is surely one of the next big aims of atomic/ionic simulators as mentioned in Ref.¹⁰, the feat is, nonetheless, yet to be achieved.

Verification of the volume law is not only of fundamental importance. If the entanglement growth can be controlled and optimised, it could unlock the potential of many-body systems as on-chip entanglers for quan-

tum networking^{6,14}. The same high degree of control also enables its usage as ballistic quantum wires^{15–19} and computers²⁰. This degree of control in entanglement generation is yet to be achieved in any quantum simulator.

Photonic circuits have been used for realising varied phenomena such as bosonic and fermionic quantum walks^{21,22}, quantum-classical differences in complexity^{23–26}, quantum chemistry²⁷ and localization in transport²⁸. The ground states of some few-body spin systems^{29–31}, as well as some analogues of quantum state transfer (QST) through spin chains using coherent optics^{32,33}, have been realised in photonics. In this article, we report two firsts in the general area of quantum simulation of many-body dynamics. Using the photonic circuits we (i) verify the generation of extensive (volume law) entanglement from the dynamics of a spin chain, a canonical many-body system, following a quench, and (ii) demonstrate an exquisite control and optimisation of the generated entanglement, as necessary for building future devices.

Our achievements are made possible by engineering two novel photonic chips: (a) the quantum transport chip and (b) the entanglement characterization chip. The first chip is designed to implement a spin chain dynamics which generates, multiple entangled pairs of distant “simulated” spins. This pattern greatly facilitates the detection of entanglement and its volume law distribution after dynamics. Entanglement, however, is a notoriously difficult entity to detect even for single pairs and require local measurements in at least two non-commuting bases. Thus we design the second chip which directly interferes distant output modes of the first chip to make entanglement detection feasible through photon counting. This

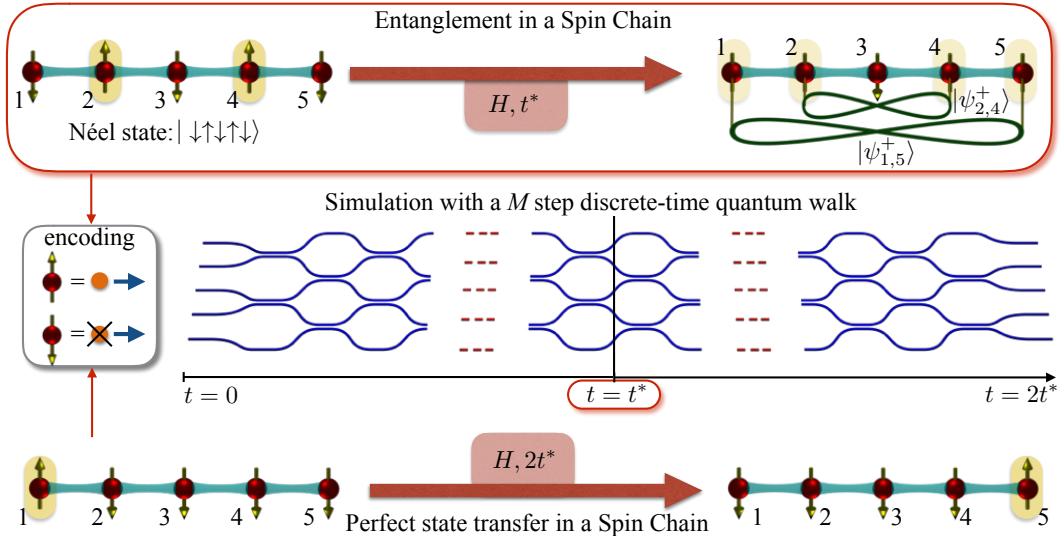


FIG. 1. Quantum simulation of spin chain dynamics and the entanglement growth therein in photonic platforms. Fermions simulated on the network map, via the Jordan-Wigner transformation, to spin excitations in a chain: occupied and unoccupied modes correspond respectively to spin up and spin down. The couplings of the effective spin chain Hamiltonian are so engineered as to generate, starting from a Néel state, at a time t^* , a state with maximal entanglement between distant symmetric sites with respect to the center of the chain. $|\psi_{i,j}^+\rangle$ stands for a maximally entangled state of spins in sites i and j . This rainbow state exhibits a volume law entanglement in which the entanglement between the left and the right halves of the chain is $\sim N/2$. The time evolution is approximated through a set of discrete steps (a digital approach). If the dynamics was continued up to time $2t^*$, it would implement an approximately perfect QST.

second chip will have a versatile application as a detector of entanglement from the outputs of any other future chips that implement other (generic) spin chain dynamics.

THEORY

Through our quantum transport chip, we simulate the dynamics induced by a “quantum quench” – a process in which the interactions inside a many-body system are suddenly changed. Let us consider preparing initially the famous Néel state $|\psi_{\text{Neel}}\rangle = |\downarrow\uparrow\downarrow\ldots\uparrow\downarrow\rangle$ of simulated spins, which is the ground state of the antiferromagnetic Ising chain and manifestly has no entanglement between any pairs of spins (the whole state is a separable state). In a condensed matter scenario, this state would be prepared by cooling under a Ising Hamiltonian. In photonic technology, we simply inject our apparatus with a simulated Néel state as to be described later. Immediately following the injection, the state starts evolving in accordance to the Hamiltonian simulated by our chip. This corresponds to the archetypical (perhaps the most extensively theoretically studied) spin chain quench^{6,14,34,35} in which the system Hamiltonian is suddenly changed from the Ising model to the XY model

$$H = \sum_{i=1}^{N-1} \frac{1}{2} J_i (X_i X_{i+1} + Y_i Y_{i+1}) \quad (1)$$

where X_i, Y_i represent the Pauli matrices for the spin in the site i and N is the length of the chain. Further, the photonics platform enables us to set the $J_i = \sqrt{i(N-i)}$ (which has not yet been feasible in the atomic/ionic platforms for quench). Then one generates, after a relevant time t^* , a remarkable pattern of nested entangled states^{6,36}, also dubbed as “rainbow states”³⁷ (cf Fig.1):

$$|\psi_{v.l.}\rangle = |\psi_{1,N}^+\rangle |\psi_{2,N-1}^+\rangle \dots \quad (2)$$

where $|\psi_{i,j}^+\rangle = \frac{1}{\sqrt{2}}(|\uparrow_i\downarrow_j\rangle + |\downarrow_i\uparrow_j\rangle)$. This state corresponds to a “volume law” for entanglement as the number of entangled pairs is $\sim N/2$ (exactly $N/2$ for even N and $(N-1)/2$ for the odd N). In other words, the amount of entanglement between the left and the right halves of the spin chain generated due to the quench dynamics scales as the size $\sim N/2$ of each part. Even more strikingly, it corresponds to the maximal entropy of entanglement, a much discussed quantity in recent theory and experiment¹⁰, between the left and the right blocks of the spin chain. Remarkably, at time $2t^*$ the system implements a perfect QST¹⁶ and thus returns to its original separable state.

Our simulation technique combines three principal ingredients. Firstly, using the Jordan-Wigner transformation^{1,3,6,14} it is possible to map spin excitations in a chain with nearest-neighbour interactions onto non-interacting fermions hopping in a lattice (hence the name quantum transport chip). Secondly, fermionic behaviour can be simulated in photonic platforms using two-photon entangled states with antisymmetric wave-

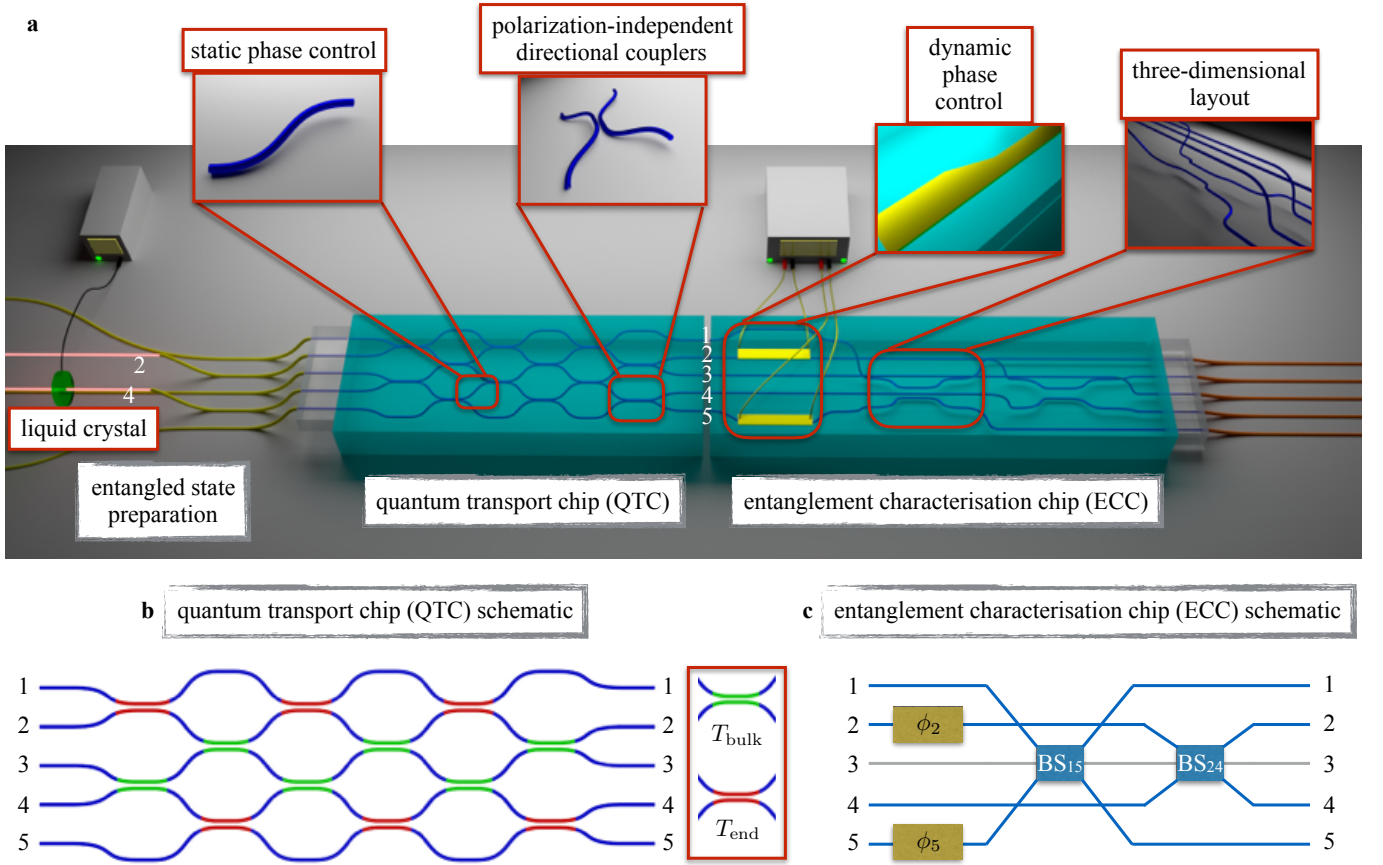


FIG. 2. **a.** Representation of the experimental apparatus comprised of the first quantum transport chip and the second entanglement characterisation chip. The insets highlight the specific elements and the three dimensional geometry of the photonic devices. **b.** Schematisation of the quantum transport device of the first chip showing in green the directional couplers of the bulk (with transmissivity $T_{\text{bulk}} = 0.36$) and in red those at the edge (with transmissivity $T_{\text{end}} = 0.25$) of the device. **c.** Schematic representation of the entanglement characterisation device of the second chip, showing the dynamic phase controls ϕ_2 and ϕ_5 acting on the 2nd and 5th waveguides and the 50/50 beam splitters between the (2,4) and (1,5) pairs of modes. The 3rd waveguide (in grey) is not involved in any interference processes.

functions; this has already been exploited for simulating several phenomena, such as Bosonic-Fermionic continuous transition^{21,22}, Anderson localisation²⁸ and Fano interference effect in quantum decay³⁸. Third is the fact that while the spin chain dynamics maps effectively to a continuous time quantum walk of multiple fermions it can be simulated via discrete quantum walks in the weak transmission limit³⁹. Discrete quantum walks provide more accurate control over the implemented Hamiltonian⁴⁰ due to the additional degree of freedom given by the coin operator. An N -sites continuous quantum walk with site-to-site coupling J_i can be simulated by a photonic network constituted by M layers of beamsplitters in cascade (see Fig. 1) with transmissivities $T_i = \sin^2(\epsilon J_i)$, where the scaling factor $\epsilon = \frac{N+1}{M} = \frac{2t^*}{M}$ should be small to be in the weak transmission limit, which means that the approximation will be more accurate with a larger number of steps. In essence, this third ingredient is thus a digital approach to quantum simulations as recently undertaken in super-

conducting networks⁴¹. Further details on the theoretical model are provided in the Supplementary Information.

EXPERIMENTS

In our work, the quantum transport chip is a 5-sites, 6-steps integrated interferometer with engineered couplings for approximating the dynamical generation of the rainbow state of Eq. (2) which displays the volume law. We studied the evolution of a two-particle fermionic states (equivalent to the Néel state of a 5 site antiferromagnet) and its bosonic counterpart, analysing the different statistics at the output and confirming the prediction for creation of the rainbow pattern of entanglement in the fermionic case. This has been possible by merging several experimental techniques, such as entanglement generation in bulk optics, state propagation in polarisation-insensitive integrated circuits, and entanglement analysis in a 3D tuneable integrated circuit.

Optical Circuits Fabrication. The Quantum Transport Chip (QTC) consists of 5 waveguides that form a series of cascaded directional couplers (Fig. 2a). Each waveguide represents a spin particle and the directional couplers operate as the integrated equivalent of beam splitters discretising the interactions between the spins. The presence of a photon in one waveguide encodes the spin state $|\uparrow\rangle$ while the absence of a photon represents $|\downarrow\rangle$.

In order to properly reproduce the discrete time quantum state transfer it is required to use two different transmission values, $T_{\text{bulk}} = 0.36$ and $T_{\text{end}} = 0.25$, for the internal and the external beam splitters respectively (see Fig. 2b and Supplementary Information). This can be achieved by increasing the separation between the two waveguides in the interaction region of the external couplers.

The spin chain will be initiated using two photons prepared in a polarisation entangled state (see below). The chip needs to be polarisation insensitive so that the polarisation encoding does not directly affect the propagation of the two-photon state. By fabricating the couplers in a tilted geometry the transmissivity is equal for both horizontal and vertical polarisation²¹.

The Entanglement Characterisation Chip (ECC) is a device designed to collect and interfere the outgoing signals from the QTC, allowing the evaluation of the entanglement that is generated in the latter (as seen in Fig. 2a). It consists of two polarisation insensitive directional couplers formed by waveguides 1-5 & 2-4 that collect and interfere the corresponding outputs from the first device, and two heating elements fabricated over waveguides 2 and 5 in order to scan the interference fringes by modulating the phase (Fig. 2c)^{42,43}.

The ECC adopts a fully three-dimensional design. The waveguides start at a shallow depth of 25 μm on the collection side so the heating elements will operate efficiently. Then they go deeper at 65 μm to form the couplers without any physical crossing of the waveguides (see Fig. 2a inset). The central waveguide is not interacting with any other one.

Measurements and Results. The simulation of the spin chain dynamics on the photonic platform has been performed by exploiting polarisation-entangled pairs of photons, generated by type-II parametric downconversion process in a BBO (beta barium borate) crystal. The general expression for the state of the generated photons can be written as $|\Psi_{2p}^{\chi}\rangle = 2^{-1/2}(|HV\rangle + e^{i\chi}|VH\rangle)$, where the subscript 2p indicates a two-photon state. The phase parameter χ can be controlled by means of an electrically configurable liquid crystal positioned on one of the two photon paths. Thus both bosonic and fermionic statistics can be simulated by using the Bell states $|\Psi_{2p}^{+}\rangle$ and $|\Psi_{2p}^{-}\rangle$ respectively for their symmetric and anti-symmetric wavefunctions^{21,44}.

The Néel state $|\downarrow\uparrow\downarrow\uparrow\downarrow\rangle$ of the spin chain was simulated by injecting the polarisation-entangled state $|\Psi_{2p}^{-}\rangle$ in the inputs 2 and 4 of the QTC (see Fig. 2a-b) through a single mode fiber array and, after evolution into the

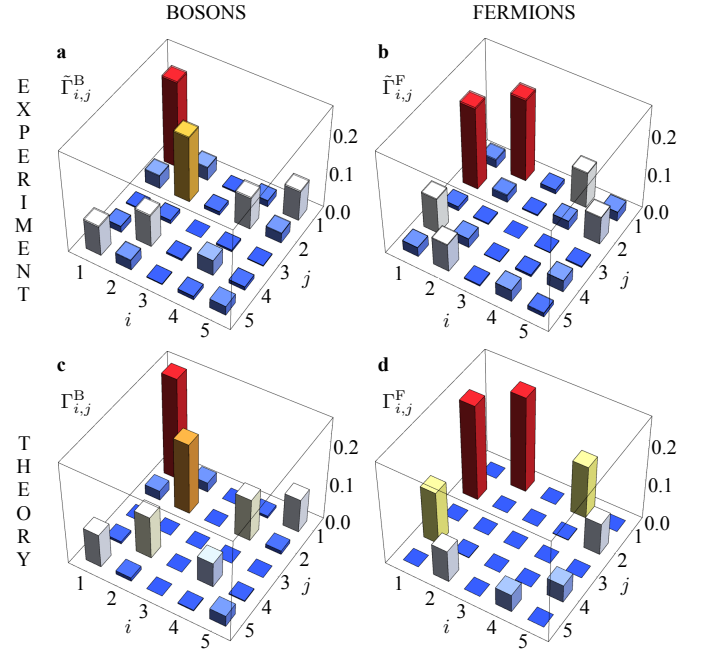


FIG. 3. **a-b.** Experimental results of the correlation function, $\tilde{\Gamma}_{ij}$, for bosonic and fermionic transport. **c-d.** Theoretical prediction for the correlation function, for bosonic and fermionic transport obtained from the unitary matrix U of the transport device.

interferometers, photons are collected via a multimode fiber array and sent to single photon avalanche photodiodes (APDs). At the output we collect coincidence measurements from all pairs of outputs to measure the off-diagonal elements (outputs $i \neq j$); for the diagonal contributions (outputs $i = j$) an in-fiber beam-splitter is inserted in each single output mode. The same experiment is also performed with $|\Psi_{2p}^{+}\rangle$ to capture the distinctive features of bosonic and fermionic dynamics on the QTC.

In the limit of a QTC with an infinite number of steps, one would expect a perfect generation of the entangled state of the form (2) exhibiting the volume law at t^* . A device with 6 steps (whose unitary we denote U), when injected with a Néel state, would give unbalanced $|\psi^{+}\rangle$ states at symmetric sites (see below). Finally, one has to take into account imperfections of the implemented unitary, by considering also the possible slight difference when acting on photons with different polarisations (\tilde{U}_H and \tilde{U}_V).

As a first step, tomographic reconstruction of the unitary transformation matrix has been performed for both polarisations H and V , which gave fidelities with respect to the expected unitary of $\mathcal{F}^H = 0.962 \pm 0.001$ and $\mathcal{F}^V = 0.977 \pm 0.002$, proving the high quality and the polarisation independence of the device (see Supplementary Information for more details on the unitary characterisation).

The results of the quantum dynamics are shown in Fig.

3 for both bosonic and fermionic behavior, where the experimental ($\tilde{\Gamma}_{ij}^{B/F}$) and theoretical ($\Gamma_{ij}^{B/F}$, calculated from the 6-steps unitary U) correlation functions^{45,46} are reported. The output probabilities detected experimentally are related to the correlation function by the equations $\tilde{\Gamma}_{ii} = P_{ii}$ and $\tilde{\Gamma}_{ij} = \frac{P_{ij}}{2}$, due to the symmetrisation of the correlation function matrix.

From the results shown in Fig. 3 one can observe the different bosonic and fermionic evolution: for states which are symmetric with respect to particle exchange, the bosonic distribution has a strong contribution on the diagonal terms of the matrix, which is a clear sign of the bosonic coalescence; for the anti-symmetric state, the resulting fermionic evolution gives strong contributions on the off-diagonal terms of the matrix.

Each experimental distribution is compared to its theoretical prediction through the measurement of the similarity, with results for the bosonic and fermionic transport of $\mathcal{S}^B = 0.942 \pm 0.005$ and $\mathcal{S}^F = 0.836 \pm 0.004$.

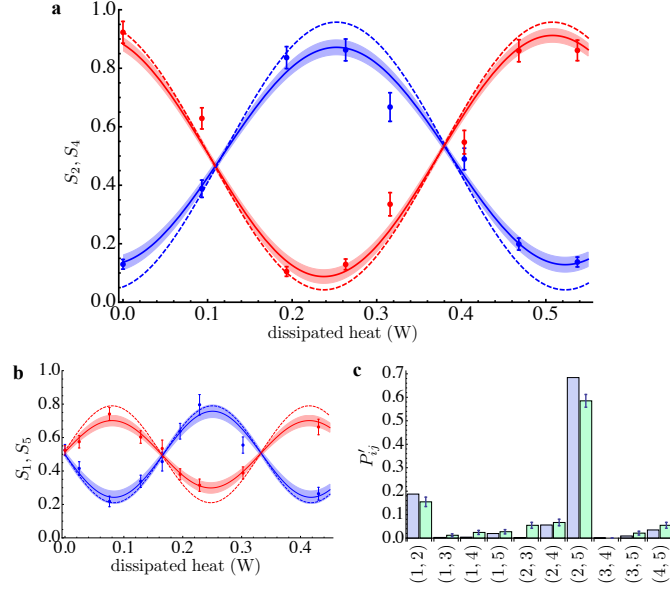


FIG. 4. Interference fringes for S_2 (blue points) and S_4 (red points) as a function of the dissipated heat on mode 2 (proportional to ϕ_2). **b.** Interference fringes for S_1 (blue points) and S_5 (red points) as a function of the dissipated heat on mode 5 (proportional to ϕ_5). In both sub-panels **a** and **b**, solid lines and shaded areas represent respectively the best fit curves and fit curve error, while the dashed lines corresponds to theoretical predictions. **c.** Green bars: two-photon probability distribution obtained at the output of the second chip, when the polarisation-entangled anti-symmetric state is injected into input 2 and 4 of the first chip. The distribution is obtained for values of the two phases which maximise P'_{25} ; blue bars: theoretical predictions. All theoretical models are obtained taking into account the reconstructed matrices of the first chip (\tilde{U}_H and \tilde{U}_V) and the coupling efficiencies at the interface between the two devices (see Supplementary Information).

Entanglement Certification. The time evolution of the state $|\Psi_{2p}^-\rangle_{24}$ (which simulates the Néel state) through an effective Hamiltonian of the form (1) acting on simulated spins gives a state equal to $|\psi_{1p}^+\rangle_{15}|\psi_{1p}^+\rangle_{24}|0\rangle_3$ at time t^* , where $|\psi_{1p}^+\rangle_{ij}$ denotes the one-photon path-encoded Bell state $|\psi^+\rangle$ over the modes i and j ⁴⁷. This state simulates the volume law entangled state $|\psi_{v,1}\rangle$ of Eq.(2). As we perform the evolution with a finite number of steps, we get a state of the form $|\psi_{out}\rangle = (\alpha|10\rangle_{15} + \beta|01\rangle_{15})(\gamma|10\rangle_{24} + \delta|01\rangle_{24})|0\rangle_3$. The imbalance between α and β and between γ and δ , which can be observed in Fig. 3, comes from the fact that a finite number of discrete step is an approximation of a perfect state transfer. To check the coherence between the terms $|10\rangle_{ij}$ and $|01\rangle_{ij}$, a phase shift and a beamsplitter transformation over the modes i and j can be applied, where $(i, j) = (1, 5)$ and $(2, 4)$. This transformation is implemented in the ECC device (see Fig. 2c).

We first measured the two-photon interference fringes obtained by varying the phases ϕ_2 and ϕ_5 . More specifically, we defined the quantities S_i (see Methods) which depend only from the tuning of a single phase, while being insensitive to possible cross-talks over neighbouring modes due to heat dispersion. Interference fringes, shown in Fig. 4a-b, are clearly visible when plotting S_1 and S_5 (S_2 and S_4) as a function of ϕ_5 (ϕ_2).

To further characterise the degree of entanglement, we evaluated the *entanglement fraction* of systems 1-5 and 2-4 with respect to the ideal one-photon Bell state $|\psi_{1p}^+\rangle$: $\mathcal{E}_{ij} = {}_{ij}\langle\psi_{1p}^+|\rho_{ij}|\psi_{1p}^+\rangle_{ij}$, where ρ_{ij} is the reduced density matrix for two qubits in positions i and j ⁴⁸. These quantities can be evaluated by measuring the single-photon probabilities N'_i and two-photon probabilities P'_{ij} after evolution through the second device. Indeed, one can find that $\mathcal{E}_{15} = N'_5 - P'_{15}$ and $\mathcal{E}_{24} = N'_2 - P'_{24} - P'_{23} + P'_{34}$ (See Supplementary Information). The first expression implies finding a photon in mode 5 and no photons in mode 1. The second one keeps nonlocal terms from the mapping from spin excitations to fermions, which in the case of \mathcal{E}_{15} are factorised into a fixed phase term. By evaluating the entanglement fractions from the two-photon probabilities shown in Fig. 4c we obtain $\mathcal{E}_{15} = 0.66 \pm 0.03$ and $\mathcal{E}_{24} = 0.74 \pm 0.03$. This amounts to an approximate verification of Eq.(2) and thereby the growth of entanglement to a volume law.

CONCLUSIONS AND DISCUSSION

Using integrated photonics we have achieved the first quantum simulation of the extensive growth of entanglement in a spin chain after a quench. The volume law for the amount of entanglement between the two halves of the spin chain after an appropriate time t^* is verified. While atomic simulators have the verification of the above as one of the chief items in their future roadmap¹⁰, the exquisite control of couplings offered by integrated

photonics has made it already feasible. Moreover, our methodology of designing the QTC, in particular, a time discretisation of the dynamics that we exploit, makes it amenable to alter the chip design to simulate a wide range of such spin chain dynamics – e.g., time dependent quantum control⁴⁹, and, if some nonlinearities can be potentially introduced to the waveguides⁵⁰, then a much wider range of spin Hamiltonians such as isotropic models. The ECC, on the other hand, is versatile – it will enable a detection of the entangled outputs from any of the above range of spin chain dynamics that can be accomplished in integrated photonics. In the future, scaling to larger spin chains should also be possible with fully antisymmetric states of more photons²², for example using additional degrees of freedom, mimicking more fermions. The entanglement growth we have observed is responsible for thermalisation in systems that do thermalise, and also corresponds to the formation of a black hole through the holographic correspondence. Aside this fundamental interest, the level of control shown by the generation of the rainbow states with a high entangled fraction, will make integrated photonics an ideal platform to benchmark and optimise quantum nano-devices of the future.

METHODS

Devices fabrication technique. In both chips, the QTC and the ECC, the waveguides are inscribed by femtosecond laser writing in Corning Eagle-2000 borosilicate glass. We used a femtosecond Yb:KYW cavity-dumped oscillator at 1030 nm wavelength, emitting pulses with 300 fs duration, and at a 1 MHz repetition rate. The laser beam was focused through a 50x, 0.6 NA microscope objective lens into the glass substrate, which was translated by a computer-controlled three-axis Aerotech FiberGlide 3D series stage, at a velocity of 40 mm/s. In

the QTC the waveguides are inscribed using 220 mW of laser power at a depth of 170 μm . In the ECC the power of inscription was slightly lower at 210 mW since the waveguides were closer to the surface.

QTC characterisation. After fabrication, the circuit was characterised classically using a diode laser. The overall performance was verified by collecting the output power distribution for each individual input and comparing it to the theoretically expected one. The polarisation response of the chip was identical for both vertical and horizontal polarisations within 2%, and the similarity between the theoretically expected and experimentally measured output distributions were $\mathcal{S}^H = 0.963 \pm 0.002$ and $\mathcal{S}^V = 0.976 \pm 0.002$.

ECC characterisation. Before using the ECC in the actual quantum experiment, the device was characterised independently by coupling it to a chip containing balanced directional couplers, thus forming Mach-Zehnder interferometers. By applying different voltages to the heating electrodes it was possible to observe the interference fringes at the output of the corresponding interferometers with visibilities $V_{1-5} = 0.86 \pm 0.02$ and $V_{2-4} = 0.94 \pm 0.02$ (for an expect value of $V_{i-j} = 1$). In addition, we verified the stability of the thermal tuning of the phase and we have observed that a constant phase value could be maintained for a period of 8 hours with a standard deviation $\sigma_\Phi = |0.03|$ radians.

Interference fringes measurement. Let us define $S_1 = P'_{12} + P'_{14}$, where P'_{ij} is the two-photon probability at the outputs i and j of the second device. Such quantity depends only from the tuning of phase ϕ_5 on mode 5, while being insensitive to possible thermal cross-talks between the modes. Analogous quantities can be defined for modes 2, 4 and 5 ($S_2 = P'_{21} + P'_{25}$, $S_4 = P'_{41} + P'_{45}$ and $S_5 = P'_{52} + P'_{54}$). The recorded visibilities were $V_{S_1} = 0.51 \pm 0.05$, $V_{S_5} = 0.40 \pm 0.03$, $V_{S_2} = 0.74 \pm 0.03$, and $V_{S_4} = 0.82 \pm 0.03$.

* s.bose@ucl.ac.uk

† roberto.osellame@polimi.it

‡ fabio.sciarrino@uniroma1.it

¹ Polkovnikov, A., Sengupta, K., Silva, A. & Vengalattore, M. Nonequilibrium dynamics of closed interacting quantum systems. *Rev. Mod. Phys.* **83**, 863 (2011).

² Feynman, R. P. Simulating physics with computers. *Int. J. Theor. Phys.* **21**, 467-488 (1982).

³ Calabrese, P., & Cardy, J. Evolution of entanglement entropy in one-dimensional systems. *J. Stat. Mech.*, P04010 (2005)

⁴ Altman, E. & Vosk, R. Universal dynamics and renormalization in many-body localized systems. *Annual Review of Condensed Matter Physics* **6**, 383-409 (2015).

⁵ Bardarson, J. H., Pollmann, F. & Moore, J.E. *Phys. Rev. Lett.* **109**, 017202 (2012).

⁶ Alkurtass, B., Banchi L. & Bose S. Optimal quench for distance-independent entanglement and maximal block entropy. *Phys. Rev. A* **90**, 042304 (2014).

⁷ Eisert, J., Friesdorf, M. & Gogolin C. Quantum many-body systems out of equilibrium. *Nature Phys.* **11**, 124-130 (2015).

⁸ Takayanagi, T. & Ugajin, T. Measuring the black hole formation by entanglement entropy via coarse-graining. *JHEP* **11**, 1-23 (2010).

⁹ Liu, H. & Suh, S. J. Entanglement tsunami: universal scaling in holographic thermalization. *Phys. Rev. Lett.* **112**, 011601 (2014).

¹⁰ Islam, R. *et al.* Measuring entanglement entropy in a quantum many-body system *et al.*, *Nature* **528**, 77-83 (2015).

¹¹ Jurcevic, P. *et al.* Quasiparticle engineering and entanglement propagation in a quantum many-body system. *Nature* **511**, 202-205 (2014).

¹² Richerme, P. *et al.* Non-local propagation of correlations in quantum systems with long-range interaction. *Nature* **511**, 198-201 (2014).

¹³ Fukuhara, T. *et al.* Spatially resolved detection of a spin-entanglement wave in a Bose-Hubbard chain. *Phys. Rev.*

- Lett.* **115**, 035302 (2015).
- ¹⁴ Wichterich, H. & Bose, S. Exploiting quench dynamics in spin chains for distant entanglement and quantum communication. *Phys. Rev. A* **79**, 060302(R) (2009).
 - ¹⁵ Bose, S. Quantum communication through an unmodulated spin chain. *Phys. Rev. Lett.* **91**, 207901 (2003).
 - ¹⁶ Christandl, M., Datta, N., Ekert, A., & Landahl, A. Perfect state transfer in quantum spin networks. *Phys. Rev. Lett.* **92**, 187902 (2004).
 - ¹⁷ Banchi, L., Apollaro, T. J. G., Cuccoli, A., Vaia, R., & Verrucchi, P. Optimal dynamics for quantum-state and entanglement transfer through homogeneous quantum systems. *Phys. Rev. A* **82**, 052321 (2010).
 - ¹⁸ Yao, N. Y. *et al.* Robust quantum state transfer in random unpolarized spin chains. *Phys. Rev. Lett.* **106**, 040505 (2011).
 - ¹⁹ Banchi, L., Bayat, A., Verrucchi, P. & Bose, S. Nonperturbative entangling gates between distant qubits using uniform cold atom chains. *Phys. Rev. Lett.* **106**, 140501 (2011).
 - ²⁰ Feynman R. P. Quantum mechanical computers. *Opt. News* **11**, 11-20 (1985).
 - ²¹ Sansoni, L. *et al.* Two-particle bosonic-fermionic quantum walk via integrated photonics. *Phys. Rev. Lett.* **108**, 010502 (2012).
 - ²² Matthews, J. *et al.* Observing fermionic statistics with photons in arbitrary processes. *Sci. Rep.* **3**, 1539 (2013).
 - ²³ Broome, M. A. *et al.* Photonic Boson Sampling in a Tunable Circuit. *Science* **339**, 794-798 (2013).
 - ²⁴ Spring, J. B. *et al.* Boson Sampling on a Photonic Chip. *Science* **339**, 798-801 (2013).
 - ²⁵ Tillmann, M. *et al.* Experimental boson sampling. *Nature Photon.* **7**, 540-544 (2013).
 - ²⁶ Crespi A. *et al.* Integrated multimode interferometers with arbitrary designs for photonic boson sampling. *Nature Photon.* **7**, 545-549 (2013).
 - ²⁷ Peruzzo, A. *et al.* A variational eigenvalue solver on a photonic quantum processor. *Nature Commun.* **5**, 4213 (2014).
 - ²⁸ Crespi, A. *et al.* Anderson localization of entangled photons in an integrated quantum walk. *Nature Photon.* **7**, 322-328 (2013).
 - ²⁹ Barz, S. *et al.* Linear-optical generation of eigenstates of the two-sites XY model. *Phys. Rev. X* **5**, 021010 (2015).
 - ³⁰ Ma, X. S. *et al.* Towards photonic quantum simulation of ground states of frustrated Heisenberg spin systems *Sci. Rep.* **4**, 3583 (2014).
 - ³¹ Orioux, A. *et al.* Experimental linear-optics simulation of multiparticle non-locality in the ground state of a quantum Ising ring. *Sci. Rep.* **4**, 7184 (2014).
 - ³² Bellec, M., Nikolopoulos, G. M. & Tzortzakakis, S. Faithful communication Hamiltonian in photonics lattices. *Opt. Lett.* **37**, 4504 (2012).
 - ³³ Perez-Leija, A. *et al.* Coherent quantum transport in photonic lattices. *Phys. Rev. A* **87**, 012309 (2013).
 - ³⁴ De Chiara, G., Montangero, S., Calabrese, P. & Fazio, R. Entanglement entropy dynamics of Heisenberg chains. *J. Stat. Mech.*, P03001 (2006).
 - ³⁵ Barmettler, P., Punk, M., Gritsev, V., Demler, E., & Altman, E. Relaxation of antiferromagnetic order in spin-1/2 chains following a quantum quench. *Phys. Rev. Lett.* **102**, 130603 (2009).
 - ³⁶ Di Franco, C., Paternostro, M., & Kim M. S. Nested entanglement states for distributed quantum channels. *Phys. Rev. A* **77**, 020303(R) (2008).
 - ³⁷ Ramírez, G., Rodríguez-Laguna, J. & Sierra, G. Entanglement over the rainbow. *J. Stat. Mech.*, P06002 (2015).
 - ³⁸ Crespi, A., *et al.* Particle statistics affects quantum decay and Fano interference. *Phys. Rev. Lett.* **114**, 090201 (2015).
 - ³⁹ Strauch, F. W. Connecting the discrete- and continuous-time quantum walks. *Phys. Rev. A* **74**, 030301(R) (2006).
 - ⁴⁰ Reck, M., Zeilinger, A., Bernstein, H. J. & Bertani, P.. Experimental realization of any discrete unitary operator. *Phys. Rev. Lett.* **73**, 58-61 (1994).
 - ⁴¹ Barends, R. *et al.* Digital quantum simulation of fermionic models with a superconducting circuit. *Nature Commun.* **6**, 7654 (2015).
 - ⁴² Flamini, F. *et al.* Thermally reconfigurable quantum photonic circuits at telecom wavelength by femtosecond laser micro-machining. *Light: Science & Applications.* **4**, e354 (2015).
 - ⁴³ Chaboyer, Z., Meany, T., Helt, L. G., Withford, M. J. & Steel, M. J. Tunable quantum interference in a 3D integrated circuit. *Sci. Rep.* **5**, 9601 (2015).
 - ⁴⁴ Omar, Y, Paunković, N., Sheridan, L. & Bose, S. Quantum walk on a line with two entangled particles *Phys. Rev. A* **74**, 042304 (2006).
 - ⁴⁵ Bromberg, Y., Lahini, Y., Morandotti, R. & Silberberg, Y. Quantum and classical correlations in waveguide lattices. *Phys. Rev. Lett.* **102**, 253904 (2009).
 - ⁴⁶ Peruzzo, A. *et al.* Quantum walk of correlated particles. *Science* **329**, 5998, 1500-1503 (2010).
 - ⁴⁷ Lombardi, E., Sciarrino, F., Popescu, P. & De Martini, F. Teleportation of a vacuum-one-photon qubit. *Phys. Rev. Lett.* **88**, 070402 (2002).
 - ⁴⁸ Bennett, C. H., DiVincenzo, D. P., Smolin, J. A. & Wootters, W. K. Mixed-state entanglement and quantum error correction. *Phys. Rev. A* **54**, 3824 (1996).
 - ⁴⁹ Brif, C., Chakrabarti, R., & Rabitz, H. Control of quantum phenomena: past, present and future. *New J. Phys.* **12**, 075008 (2010).
 - ⁵⁰ Venkataraman, V., Saha, K., Gaeta, A. L. Phase modulation at the few-photon level for weak-nonlinearity-based quantum computing. *Nature Photon.* **7**, 138-141 (2013).
- Acknowledgements.** This work was supported by the Marie Curie Initial Training Network PICQUE (Photonic Integrated Compound Quantum Encoding, grant agreement no. 608062, funding Program: FP7-PEOPLE-2013-ITN, <http://www.picque.eu>) and by the H2020-FETPROACT-2014 Grant QUCHIP (Quantum Simulation on a Photonic Chip; grant agreement no. 641039, <http://www.quchip.eu>).
- Author contribution.** L.B., S.B., P.M., R.O., F.S. conceived the idea. I.P., A.C., R.O. designed and fabricated the integrated photonics devices and carried out their characterization with classical light. A.S.R., D.C., M.B., N.S., F.S. carried out the quantum experiments and analyzed the data. L.B, S.B. developed the theoretical model of engineered quantum walk and of entanglement growth. All authors discussed the experimental implementation and results, and contributed to writing the paper.
- Competing financial interests.** The authors declare no competing financial interests.
- Materials & Correspondence.** Correspondence

and requests for materials should be addressed to S.B., R.O and F.S.

Photonic Simulation of Entanglement Growth After a Spin Chain Quench

- Supplementary Information-

Ioannis Pitsios,^{1,2} Leonardo Banchi,³ Adil S. Rab,⁴ Marco Bentivegna,⁴
 Debora Caprara,⁴ Andrea Crespi,^{1,2} Nicolò Spagnolo,⁴ Sougato
 Bose,³ Paolo Mataloni,⁴ Roberto Osellame,^{1,2} and Fabio Sciarrino⁴

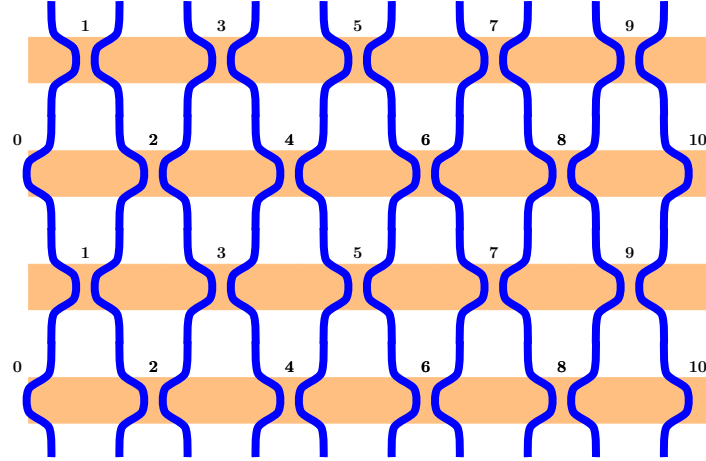
¹*Istituto di Fotonica e Nanotecnologie - Consiglio Nazionale delle Ricerche (IFN-CNR),
 P.za Leonardo da Vinci, 32, I-20133 Milano, Italy*

²*Dipartimento di Fisica - Politecnico di Milano,
 P.za Leonardo da Vinci, 32, I-20133 Milano, Italy*

³*Department of Physics and Astronomy, University College London,
 Gower Street, WC1E 6BT London, United Kingdom*

⁴*Dipartimento di Fisica - Sapienza Università di Roma, P.le Aldo Moro 5, I-00185 Roma, Italy*

DISCRETIZATION OF CONTINUOUS TIME QUANTUM WALKS



Supplementary Figure 1. Example configuration with 9 sites and 4 time steps. There are also two boundary sites 0,10. The spatial direction corresponds to the horizontal one while the “time” is the vertical direction. Light come from top to bottom. Each beam splitter is localized in a site i .

We consider a configuration as in Supplementary Fig.1 and we call $|\leftarrow\rangle$ and $|\rightarrow\rangle$ the states moving leftwards or rightwards. The left input of the beam splitter (BS) x is named $|x, \rightarrow\rangle$, while the right input is named $|x, \leftarrow\rangle$. On the other hand, the right output of BS x becomes the left

input of BS $x+1$, namely $|x+1, \rightarrow\rangle$. Similarly, the left output of BS x is $|x-1, \leftarrow\rangle$. In summary,

$$\begin{aligned} |\text{in}, x, \text{Left}\rangle &= |x, \rightarrow\rangle, & |\text{in}, x, \text{Right}\rangle &= |x, \leftarrow\rangle, \\ |\text{out}, x, \text{Left}\rangle &= |x-1, \leftarrow\rangle, & |\text{out}, x, \text{Right}\rangle &= |x+1, \rightarrow\rangle. \end{aligned} \quad (\text{S1})$$

Each beam splitter implements the transformation B , defined as $B|\text{Right}\rangle = t'|\text{Left}\rangle + r'|\text{Right}\rangle$, $B|\text{Left}\rangle = r|\text{Left}\rangle + t|\text{Right}\rangle$, so in general

$$B_x |x, \leftarrow\rangle = t'_x |x-1, \leftarrow\rangle + r'_x |x+1, \rightarrow\rangle, \quad B_x |x, \rightarrow\rangle = r_x |x-1, \leftarrow\rangle + t_x |x+1, \rightarrow\rangle. \quad (\text{S2})$$

We define the evolution operator $U = \oplus_x B_x$ generated by the series of beam splitters. This operator can be split in two terms, $U = SC$, as in the quantum walk literature, where $S = \sum_x |x-1\rangle\langle x| \otimes |\leftarrow\rangle\langle\leftarrow| + |x+1\rangle\langle x| \otimes |\rightarrow\rangle\langle\rightarrow|$ is the shift operator, and C is a *coin operator* $C|x, \leftarrow\rangle = t'_x|x, \leftarrow\rangle + r_x|x, \rightarrow\rangle$, $C|x, \rightarrow\rangle = r'_x|x, \leftarrow\rangle + t_x|x, \rightarrow\rangle$, obtained by reshuffling the beam splitter operator. By parametrizing each beam splitter operator with its transmissivity $T_x = t_x^2$ and by defining the angle Θ_x such that $T_x = \sin^2 \Theta_x$, one can show that the coin operator can be written as $C = \exp \left[i \left(\frac{\pi}{2} \mathbb{1} - \hat{\Theta} \right) \sigma^y \right]$, where $\hat{\Theta} = \sum_x \hat{\Theta}_x |x\rangle\langle x|$ and where σ^y is the Pauli matrix acting on the coin space.

To simplify the theoretical analysis we consider periodic boundary conditions. This does not affect the generality of the result and, for instance, open boundary conditions can be obtained by adding an auxiliary BS with zero transmittance, $T_{\text{Aux}} = 0$. Then it is possible to define the Fourier basis $|\tilde{p}\rangle = \frac{1}{\sqrt{N+1}} \sum_x e^{-i\tilde{p}x} |x\rangle$, $\tilde{p} = 2\pi \frac{p}{N+1}$ which diagonalizes the shift operator. Indeed, in terms of the global momentum operator $\hat{P} = \sum \tilde{p} |\tilde{p}\rangle\langle\tilde{p}|$, it is $S = \exp \left(-i\hat{P}\sigma^z \right)$. As interference effects can occur only between even/odd sites, it is convenient to study U^2 and since $e^{i\pi/2\sigma^y} e^{-i\hat{P}\sigma^z} e^{i\pi/2\sigma^y} = -e^{i\hat{P}\sigma^z}$ and $e^{-i\hat{\Theta}\sigma^y} = e^{-i\pi/2\sigma^z} e^{i\hat{\Theta}\sigma^y} e^{i\pi/2\sigma^z}$ one obtains

$$U^2 = -\exp \left(-i\hat{P}\sigma^z \right) \exp \left[-i\hat{\Theta}\sigma^y \right] \exp \left[i \left(\hat{P} - \frac{\pi}{2} \mathbb{1} \right) \sigma^z \right] \exp \left[i\hat{\Theta}\sigma^y \right] \exp \left[i \frac{\pi}{2} \mathbb{1} \sigma^z \right]. \quad (\text{S3})$$

The above exact equation is the starting point for the theoretical approximations leading to the simulation of continuous time quantum walks.

When $T_x = 1 - \epsilon_x$, with $\epsilon_x \ll 1$, the evolution generated by Eq.(S3) in the long-time and long-distance limit can be approximated by the evolution generated by a Dirac Hamiltonian [S1, S2]. This limit is somehow trivial for the purpose of quantum state transfer. Photons basically move only in one direction, since the reflectivity is negligible, and there is no complex interference phenomena.

The interesting case arises in the opposite limit $T_x \ll 1$, namely when the beam splitters have a low transmittance. In this limit, it has been shown in [S1, S2] that one can simulate a continuous time quantum walk (CTQW) with a discrete time quantum walk (DTQW). However, those mappings require both $2N$ effective sites for simulating a CTQW with N sites and also require a mixture of two types of beam splitters, one type with $T_x \approx 1$ and another set with $T_x \approx 0$. Here we use the exact Eq.(S3) to derive a simpler mapping. Using a first order expansion for small Θ_x one finds

$$U^2 \simeq -W \exp \left(i2\hat{H}\sigma^z \right) W^\dagger, \quad W = \frac{1}{\sqrt{2}} \begin{pmatrix} ie^{-i\hat{P}} & -ie^{-i\hat{P}} \\ \mathbb{1} & \mathbb{1} \end{pmatrix}, \quad (\text{S4})$$

where we have defined the Hamiltonian as $2H = e^{i\hat{P}}\hat{\Theta} + \hat{\Theta}e^{-i\hat{P}} + \mathcal{O}(\hat{\Theta}^2)$. If $\Theta_x = \epsilon j_x$ where $\epsilon \ll 1$ then

$$H \approx \frac{\epsilon}{2} \sum_x j_x |x\rangle\langle x+1| + \text{h.c.} \quad j_x \approx \frac{\Theta_x}{\epsilon} \approx \frac{\sqrt{T_x}}{\epsilon}. \quad (\text{S5})$$

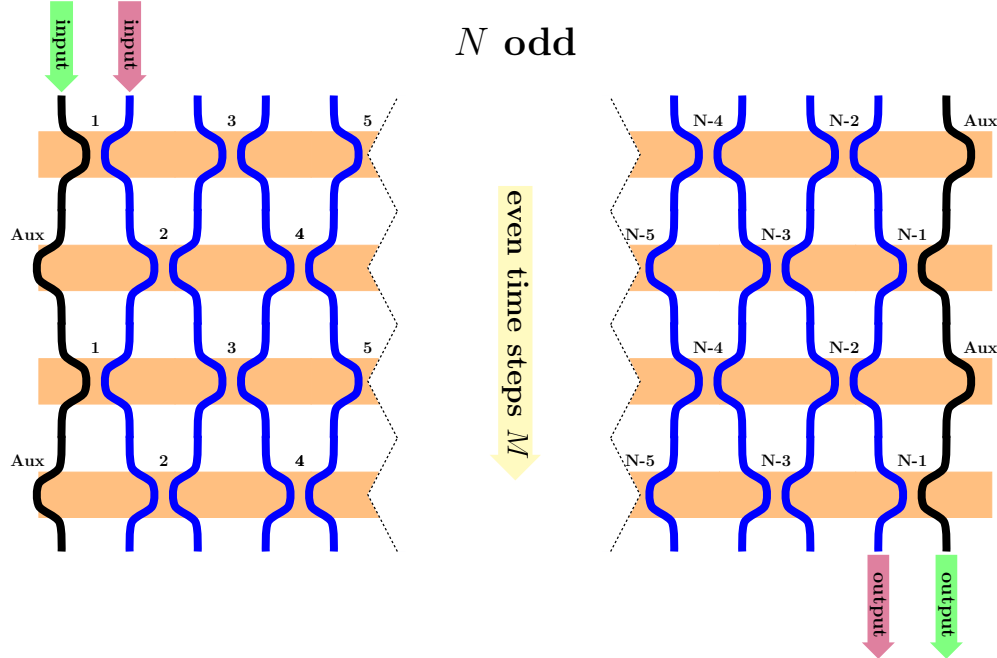
Therefore, the effective evolution reads

$$U(t) \simeq U^t = i^t W e^{it \hat{H} \sigma^z} W^\dagger . \quad (\text{S6})$$

showing that a CTQW can be approximated with a discrete time one.

DISCRETE-TIME QUANTUM TRANSPORT

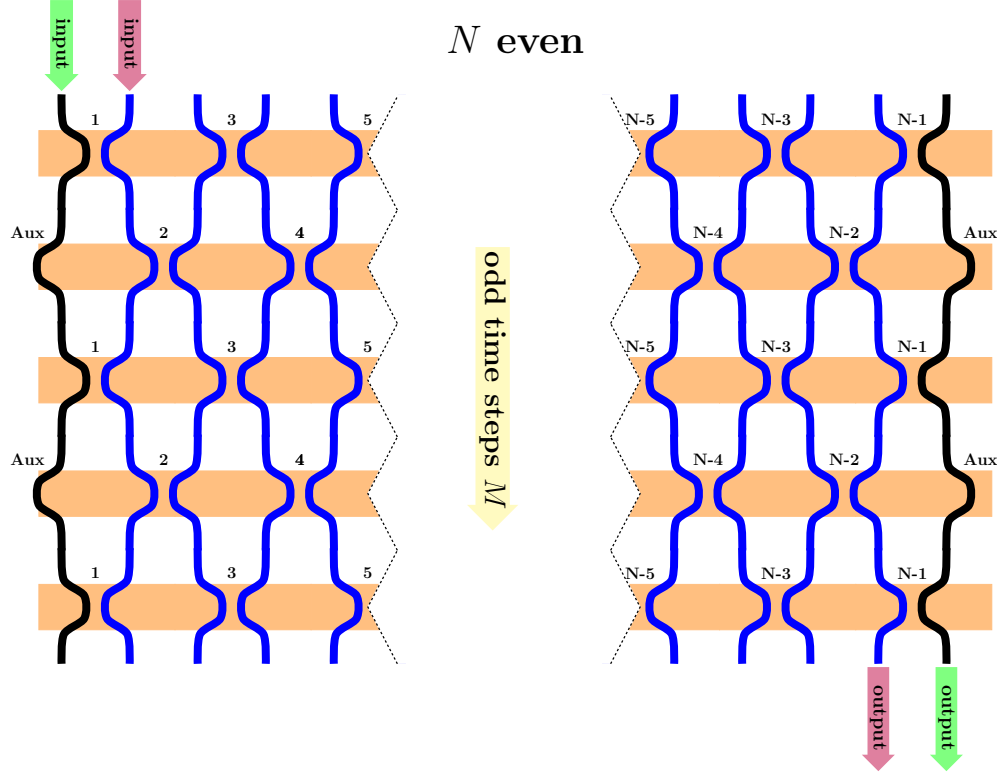
The dynamics of fully engineered chains [S3], where $j_x = \frac{\pi}{N+1} \sqrt{x(N-x)}$, $x = 1, \dots, N-1$ and N is the length of the chain, generates a perfect mirror of the initial state at the transmission time $2t^* = N+1$. Namely, every “walker” initially in position x is perfectly transferred to the position $N-x+1$, after a time $t = 2t^*$. On the other hand, minimally engineered chains [S4] require only the engineering of the transmissivity at the boundaries $j_1 = j_{N-1} = j_{\text{opt}}$, $j_x = 1$ for $x = 2, \dots, N-2$, but allow only a high-quality (almost perfect) transmission between the two ends. For large N there is an approximated formula [S4] for the optimal coupling and the transmission time: $j_{\text{opt}} = 1.030 N^{-1/6}$, while $2t^* = N+1 + 2.29 N^{1/3}$.



Supplementary Figure 2. Simulation of perfect state transfer with M time steps (M odd).

We first focus on perfect state transfer and we consider its simulation with M discrete time steps. This requires to set $2t^*/\epsilon = M$, namely

$$\epsilon = \frac{2t^*}{M} = \frac{N+1}{M} . \quad (\text{S7})$$



Supplementary Figure 3. Simulation of perfect state transfer with M time steps (M odd).

We consider an initial state in site 1 which is an arbitrary superposition of the two “coin” degrees of freedom

$$|\text{init}\rangle = \alpha|1, \rightarrow\rangle + \beta|1, \leftarrow\rangle . \quad (\text{S8})$$

When $M \gg N$, after M steps one finds

$$|\text{final}\rangle \simeq W e^{iMH\sigma^z} W^\dagger |\text{init}\rangle = \alpha|N, \rightarrow\rangle + \beta|N-2, \leftarrow\rangle . \quad (\text{S9})$$

Note that, because of the definition (S1), the states $|N, \rightarrow\rangle$ and $|N-2, \leftarrow\rangle$ correspond to the right and left output of the beam splitter in site $N-1$. The derivation presented in this section is a rigorous proof of the conjecture made in [S2] where the authors numerically observed that with fully engineered Hamiltonians (i.e. fully engineered coins) even the coin degree of freedom is perfectly transferred.

The overall scheme is presented in the Supplementary Figs. 2 and 3, both for N even and N odd. A single step moves the photon from an even site to an odd site, so an even (odd) number of time steps are required for the transmission when N is odd (even).

As one can see from the Supplementary Figs 2 and 3, $N-1$ beam splitters are required, per line, for implementing a CTQW (basically a spin chain dynamics) of N sites. Two auxiliary sets

of beam splitters, with $T_{\text{Aux}} = 0$, are required for implementing the the open boundary conditions, though the same result can also be obtained with some mirrors in the auxiliary positions 0 and N .

Theoretical simulation of state transfer with optimal couplings. When minimally engineered systems are considered, only the “right coin” state $|\rightarrow\rangle$ can be transferred. Indeed, because of the unitary operator W , the left coin state is spread between sites 1 and 2 before the transmission and, unlike fully engineered models, minimally engineered models are not able to reliably transfer a state from site 2 to site $N - 1$. For this reason, we consider only the transmission of the right coin (green light in the the Supplementary Figs 2 and 3). The transmission quality is measured via

$$Q = |\langle N, \rightarrow | U^M | 1, \rightarrow \rangle|^2, \quad (\text{S10})$$

i.e. the probability that a photon goes from $|1, \rightarrow\rangle$ to $|N, \rightarrow\rangle$ after M steps. The results are shown in terms of N (horizontal dimension), M (vertical dimension), T_{bulk} (transmittance of the beam splitters in the “bulk” $T_x = T_{\text{bulk}}$ for $x = 2, \dots, N - 2$), T_{ends} (transmittance of the beam splitters at the ends $T_x = T_{\text{ends}}$ for $x = 1, N - 1$)

| $N = 5$ | | | | $N = 6$ | | | | $N = 7$ | | | |
|---------|-------------------|-------------------|-------|---------|-------------------|-------------------|-------|---------|-------------------|-------------------|-------|
| M | T_{bulk} | T_{ends} | Q | M | T_{bulk} | T_{ends} | Q | M | T_{bulk} | T_{ends} | Q |
| 6 | 0.919 | 0.750 | 0.886 | 7 | 0.916 | 0.721 | 0.936 | 6 | 0.985 | 0.934 | 0.819 |
| 8 | 0.673 | 0.500 | 0.921 | 9 | 0.702 | 0.503 | 0.946 | 8 | 0.913 | 0.692 | 0.960 |
| 10 | 0.484 | 0.345 | 0.942 | 11 | 0.527 | 0.362 | 0.953 | 10 | 0.723 | 0.501 | 0.964 |
| 12 | 0.358 | 0.250 | 0.956 | 13 | 0.403 | 0.270 | 0.960 | 12 | 0.562 | 0.371 | 0.964 |
| 14 | 0.273 | 0.188 | 0.965 | 15 | 0.315 | 0.208 | 0.966 | 14 | 0.441 | 0.284 | 0.966 |
| 16 | 0.214 | 0.146 | 0.972 | 17 | 0.252 | 0.164 | 0.971 | 16 | 0.352 | 0.223 | 0.968 |
| 18 | 0.172 | 0.117 | 0.977 | 19 | 0.205 | 0.133 | 0.974 | 18 | 0.287 | 0.179 | 0.971 |
| 20 | 0.141 | 0.095 | 0.981 | 21 | 0.170 | 0.110 | 0.977 | 20 | 0.237 | 0.147 | 0.973 |
| 22 | 0.117 | 0.079 | 0.984 | 23 | 0.144 | 0.092 | 0.980 | 22 | 0.199 | 0.122 | 0.975 |

Note that for $N = 5$ minimally engineered models and fully engineered ones have the same coupling pattern. In particular, for a fixed transfer time step M , one can evaluate the desired coupling pattern analytically: $T_{\text{ends}} = \sin\left(\frac{2\pi}{M}\right)^2$, $T_{\text{bulk}} = \sin\left(\frac{\pi}{M}\sqrt{6}\right)^2$.

ENTANGLEMENT GROWTH AFTER A QUENCH

We consider one of the most common quenches in the spin chain literature, namely we focus on the Hamiltonian

$$\mathcal{H}_\Delta = \sum_n j_n (\sigma_n^x \sigma_{n+1}^x + \sigma_n^y \sigma_{n+1}^y + \Delta \sigma_n^z \sigma_{n+1}^z), \quad (\text{S11})$$

and we consider the quench from $\Delta = \infty$ to $\Delta = 0$. We assume that initially the system is in the ground state of \mathcal{H}_∞ , namely the Néel state $|\downarrow\uparrow\downarrow\uparrow\downarrow\uparrow\dots\rangle$, and then we effectively switch

off the parameter Δ so that the system starts to evolve according to the XY Hamiltonian \mathcal{H}_0 . One can show [S5] that when the couplings j_n are engineered for perfect state transfer, then after half the transfer time, namely after t^* , the initial state $|\downarrow\uparrow\downarrow\uparrow\downarrow\uparrow\downarrow\dots\rangle$ evolves into the state $|\psi_{1,N}^+\rangle|\psi_{2,N-1}^+\rangle|\psi_{3,N-2}^+\rangle\dots$, where $|\psi^+\rangle \propto |\uparrow\downarrow\rangle + |\downarrow\uparrow\rangle$ and the subscripts index the spins of the chain. Hence, after half the transmission time, two opposite spins lying at the same distance from the boundaries become maximally entangled. This corresponds to the creation of $N/2$ Bell pairs, namely the maximal amount of pair-wise entanglement.

In view of the Jordan-Wigner transformation, the many-spin anti-ferromagnetic initial state can be simulated using $N/2$ photons in an antisymmetric configuration. Each state $|\downarrow\rangle$ or $|\uparrow\rangle$ corresponds respectively to the absence ($|0\rangle$) or presence ($|1\rangle$) of a photon. We focus on the simplest case, i.e. when $N = 5$ and, as a consequence, the number of particles in the initial state for observing this effect is two. Writing the time evolution explicitly for bosons and fermions one can show that after half the transmission time

$$|\psi(0)\rangle = a_2^\dagger a_4^\dagger |0\rangle \longrightarrow |\psi(t^*)\rangle \propto \begin{cases} (a_1^\dagger - a_5^\dagger)(a_2^\dagger + a_4^\dagger)|0\rangle & \text{for Fermions,} \\ \left[(a_1^\dagger - a_5^\dagger)^2 + (a_2^\dagger + a_4^\dagger)^2\right] |0\rangle & \text{for Bosons.} \end{cases} \quad (\text{S12})$$

Therefore, the resulting interference pattern is completely different: while for bosons the modes are correlated pairwise (namely mode 1 with mode 5, and mode 2 with mode 4), in the fermionic case the resulting state corresponds to a delocalized particle in mode 1 and 5, and another in modes 2 and 4. Because of the Jordan-Wigner transformation, the fermionic state in (S12) corresponds to $|\psi_{1,5}^+\rangle|\psi_{2,4}^+\rangle|0\rangle$.

However, imperfections in the evolution limit the amount of entanglement between the sites. To measure the effective generated entanglement we use the entanglement fraction which, for a two-qubit state, is defined as $\mathcal{E}_{ij} = \langle\psi^+|\rho_{ij}|\psi^+\rangle$, where ρ is a two-qubit density matrix obtained by tracing all the sites but i and j . Because of (S12) we focus on \mathcal{E}_{15} and \mathcal{E}_{24} . In order to measure these quantities, we use the entanglement characterisation chip to implement the further transformations BS₁₅ BS₂₄, as described in the main text, which interfere the distant modes and allow us to measure entanglement via photodetection in terms of the expectation values

$$N'_m = \langle a_m^\dagger a_m \rangle, \quad P'_{nm} = \langle a_n^\dagger a_m^\dagger a_m a_n \rangle. \quad (\text{S13})$$

Indeed, one can show that

$$\mathcal{E}_{15} = N'_5 - P'_{51}, \quad \mathcal{E}_{24} = N'_2 - P'_{24} - P'_{23} + P'_{43}. \quad (\text{S14})$$

Eqs.(S14) give a practical way of evaluating the simulated entanglement fraction from quantities that can be measured experimentally.

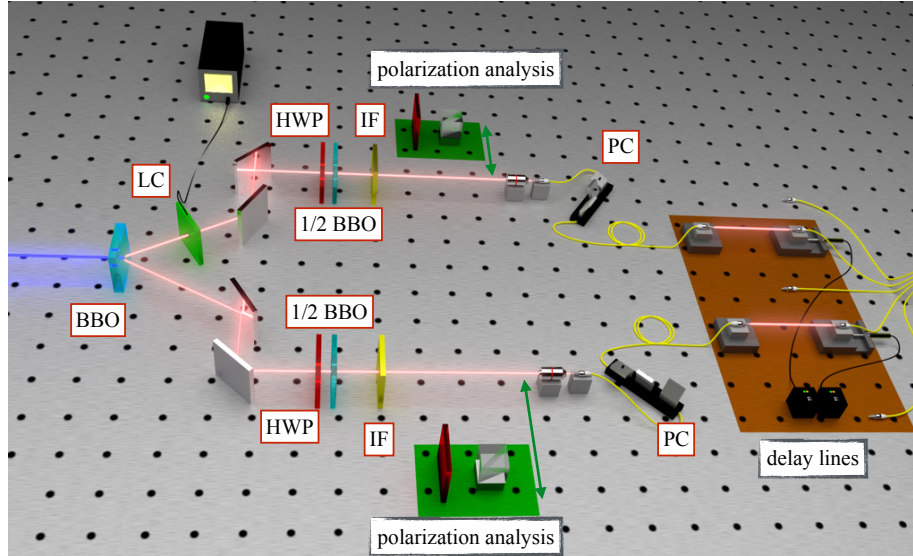
PHOTON SOURCE CHARACTERISATION

For this experiment, a mode-locked Ti:Sapphire laser with central wavelength of 785 nm, 160 fs pulse width and 76 MHz repetition rate is used as pump. Second harmonic generation (SHG) in a beta barium borate (BBO) crystal is exploited for conversion into 392.5 nm wavelength. The generation of single-photon pairs is achieved via Spontaneous Parametric Down Conversion (SPDC) by sending the converted pulses through a 2 mm-thick BBO crystal. The generated photons are spectrally filtered by means of interferential filters with 3nm bandwidth, centered at 785 nm. Typical

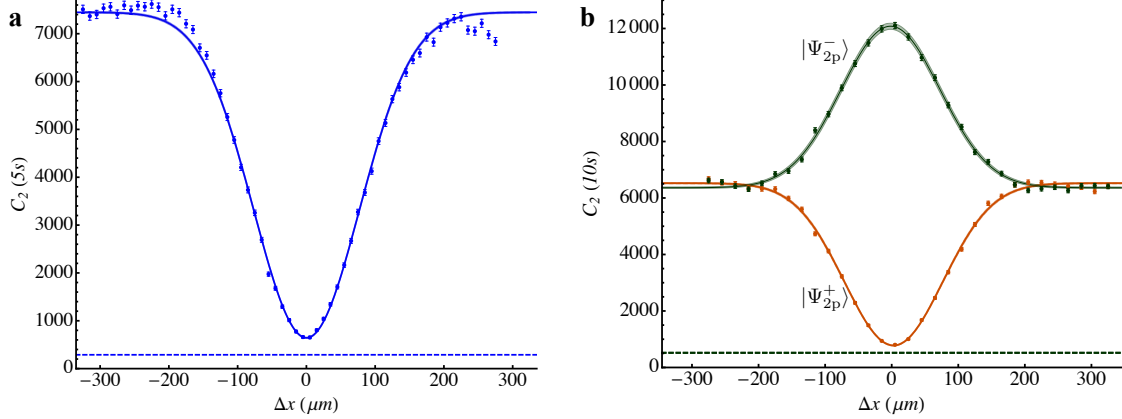
detection rates of generated photons were approximately ~ 120 KHz for singles and ~ 7 KHz for pairs. Schematics of the source is shown in Supplementary Fig. 4. The unconverted residual beam at 785 nm from the SHG is separated through a dichroic mirror and used as simulation beam for alignment and classical characterisation of the integrated device.

The generated photon state is in the general entangled form $|\Psi_{2p}^\chi\rangle = \frac{|HV\rangle + e^{i\chi}|VH\rangle}{\sqrt{2}}$, where the phase χ depends on the angle of the crystal's optical axis. Due to birefringence and dispersion effects in the SPDC BBO crystal, a walk-off compensation between the two polarizations is required for full indistinguishability. This is done by using a combination of an half-wave plate and a 1mm thick BBO crystal in each of the two photons' paths.

A controlled liquid crystal retarder is used in one arm to vary the phase χ , allowing to attain the required states. Half-wave plates and polarizing beamsplitters at each arm can be inserted when necessary to perform polarization analysis. The photons are then collected into single-mode optical fibers mounted on 3-paddle polarization controllers, used to compensate the polarization due to the bending in the fibers, and sent through delay lines to achieve temporal synchronization of the photons. Indistinguishability of the photon source is measured by performing an HOM [S6] interference experiment in a 50/50 beam splitter (BS) after polarization analysis. The obtained visibilities are $V_{\text{raw}}^{\text{source}} = -0.914 \pm 0.002$ for raw data and $V_{\text{corr}}^{\text{source}} = -0.95 \pm 0.01$ corrected for accidental counts (see Supplementary Fig 5a). Similar interference measurements have been performed for the two entangled states $|\Psi_{2p}^+\rangle$ and $|\Psi_{2p}^-\rangle$ to characterize the quality of the generated entangled. The observed visibilities where $V_{\text{raw}}^{\text{B}} = -0.880 \pm 0.002$ and $V_{\text{raw}}^{\text{F}} = 0.90 \pm 0.01$ for raw measurements, and $V_{\text{corr}}^{\text{B}} = -0.957 \pm 0.002$ and $V_{\text{corr}}^{\text{F}} = 0.97 \pm 0.01$ corrected for accidental counts (see Supplementary Fig 5b).



Supplementary Figure 4. Visual schematics of the single-photon source used for the experiment. BBO: beta barium borate crystal used for parametric down conversion; LC: liquid crystal for entanglement phase χ control; HWP & 1/2 BBO: half-waveplate and half beta barium borate crystal for walk-off compensation; PC: polarization compensation. The polarization analysis is comprised of half-waveplate and polarizing beam splitter. The delay line is used to temporally synchronize the photon and couple them into the single mode fiber array.



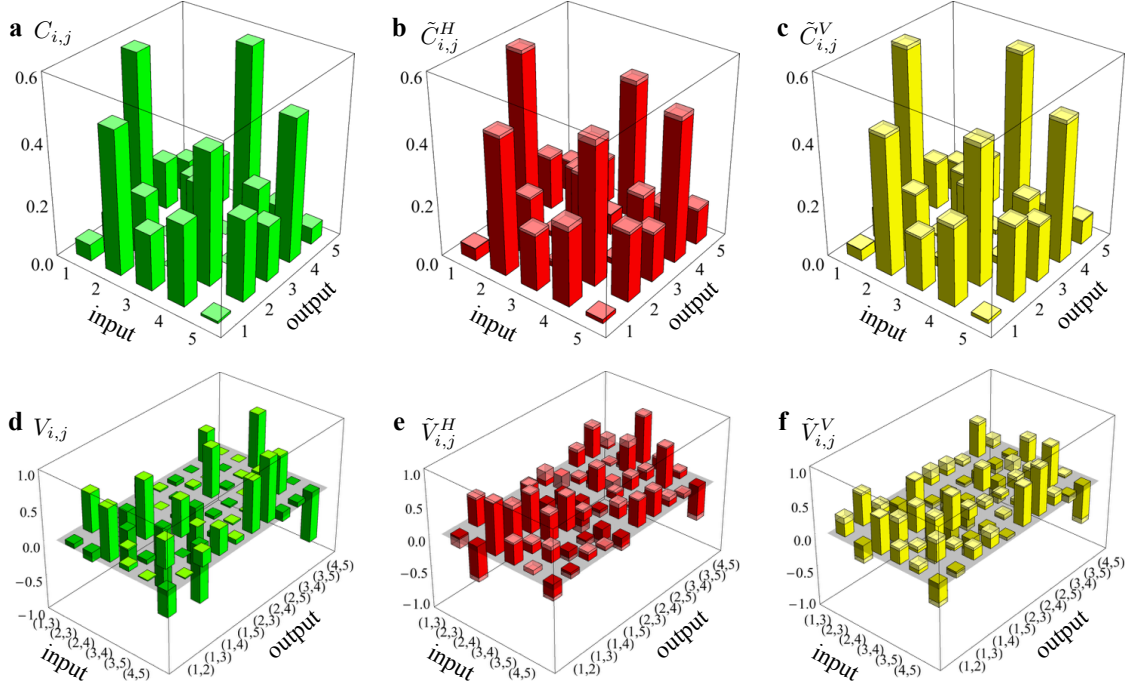
Supplementary Figure 5. **a.** Hong-Ou-Mandel interference scan over $600 \mu\text{m}$ of two indistinguishable photons. **b.** Hong-Ou-Mandel interference dip for state $|\Psi_{2p}^+\rangle$ (green) and peak for state $|\Psi_{2p}^-\rangle$ (orange).

CHARACTERISATION OF THE QTC DEVICE

The generated photons are coupled into the integrated device using a single-mode fiber array, and collected after evolution through the interferometer using a multimode fiber array which sends the photons to Single Photon Avalanche Photodiodes (SPADs). Both input and output fiber arrays are mounted on roto-translational stages. The alignment is performed using the unconverted residual from the SHG. Overall transmission efficiency from delay lines to the photodetectors with the first chip is approximately 12%, which includes transmission losses inside the chip and coupling losses at the three interfaces between delay line, input fiber array, chip and output fiber array. The phase χ of the entangled state is set by exploiting HOM interference for the output bunching contributions. This is obtained by inserting an additional in-fiber BS at output mode 1 and by measuring the output two-fold coincidences. By maximizing the coincidence rate we have a symmetric (bosonic) state $|\Psi_{2p}^+\rangle$ and by minimizing it we have an anti-symmetric (fermionic) state $|\Psi_{2p}^-\rangle$.

Photon pairs are sent into the device to simulate bosonic and fermionic transport in the lattice, respectively exploiting the symmetric and anti-symmetric nature of the Bell states $|\Psi_{2p}^+\rangle$ and $|\Psi_{2p}^-\rangle$. The simulation of the transport of a spin state in a 1D chain, initially in a Néel's state $|\downarrow\uparrow\downarrow\uparrow\downarrow\rangle$, is obtained by injecting the $|\Psi_{2p}^-\rangle$ state in input 2 and 4. Switching from one state to the other is achieved by changing the phase χ with the liquid crystal retarder. Detection of output states in which two photons are in the same spatial mode is obtained by inserting an in-fiber 50/50 beam splitter to the chip's output.

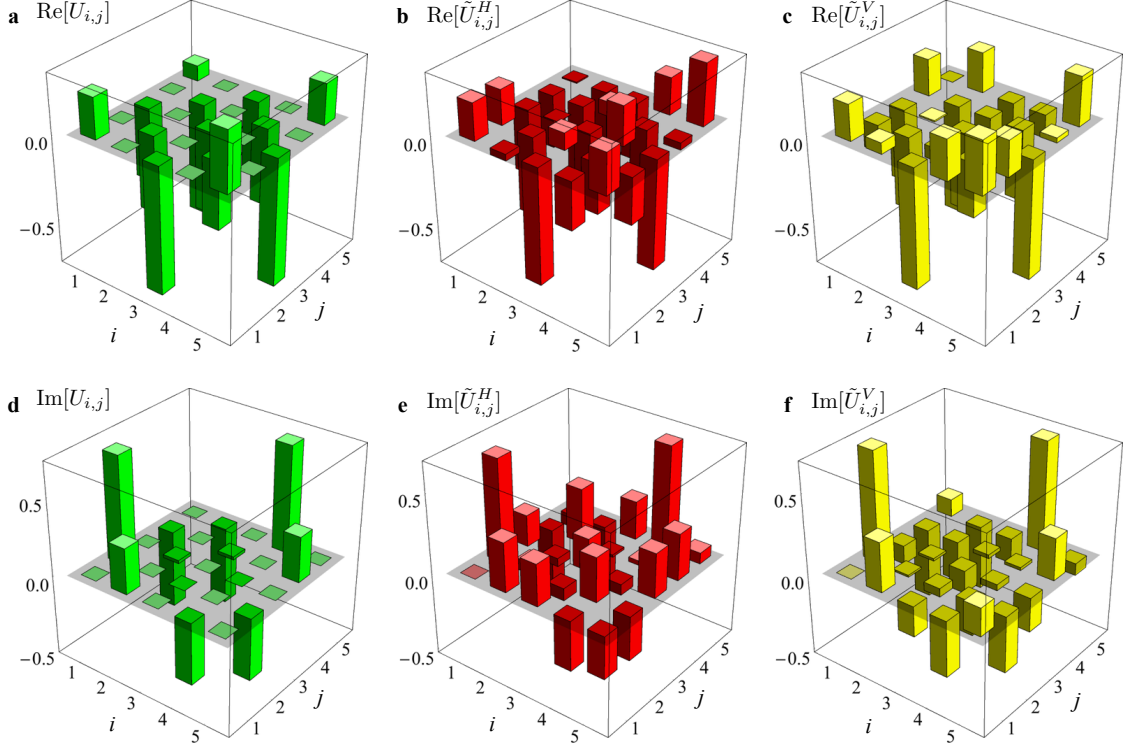
Tomography of the QTC device. The reconstruction of the unitary matrix which describes the actual interferometer corresponds to retrieving the values of its elements (moduli and complex phases). Unitary's moduli are sufficient to describe single-particle and classical behavior, while phase terms are crucial for two-particle interference. The unitary matrix is experimentally reconstructed by measuring the single-photon output distributions (or the equivalent power splitting ratios with classical light) for all inputs and two photon interference for several pairs of inputs [S7, S8]. More specifically, we measured the power splitting ratios with classical light and two-photon Hong-Ou-Mandel visibilities for 6 different input states for both polarizations H and V (see



Supplementary Figure 6. Power-splitting ratios with classical light (**a-c**) and two-photon interference dips and peaks visibilities (**d-f**) results: **a-d** calculations from the theoretical unitary U , **b-e** experimental results with horizontal polarization and **c-f** experimental results with vertical polarization. Lighter regions are 1σ experimental errors.

Supplementary Fig. 6). Characterisation of the device is performed starting from the chip structure of Fig. 1b and by assuming unknown values for all the fabrication parameters (directional couplers transmittivities and phases between the modes). The value of the parameters are obtained by minimizing a suitable χ -square function, while errors in the reconstruction are retrieved with a Monte Carlo simulation starting from the experimental power-splitting ratios and two-photon data [S8].

The obtained fidelities for the two polarizations with respect to the theoretical model are $\mathcal{F}^H = 0.962 \pm 0.001$ and $\mathcal{F}^V = 0.977 \pm 0.002$. The polarization insensitivity of the device is confirmed by the results for the fidelity between the reconstructed unitary in H and V polarization of $\mathcal{F}_{\text{Reco}}^{H/V} = 0.99 \pm 0.01$ (see Supplementary Fig. 7). Experimental single- and two-photon distributions, measured in both polarizations H and V , further confirm the polarization insensitivity (see Supplementary Fig. 8).

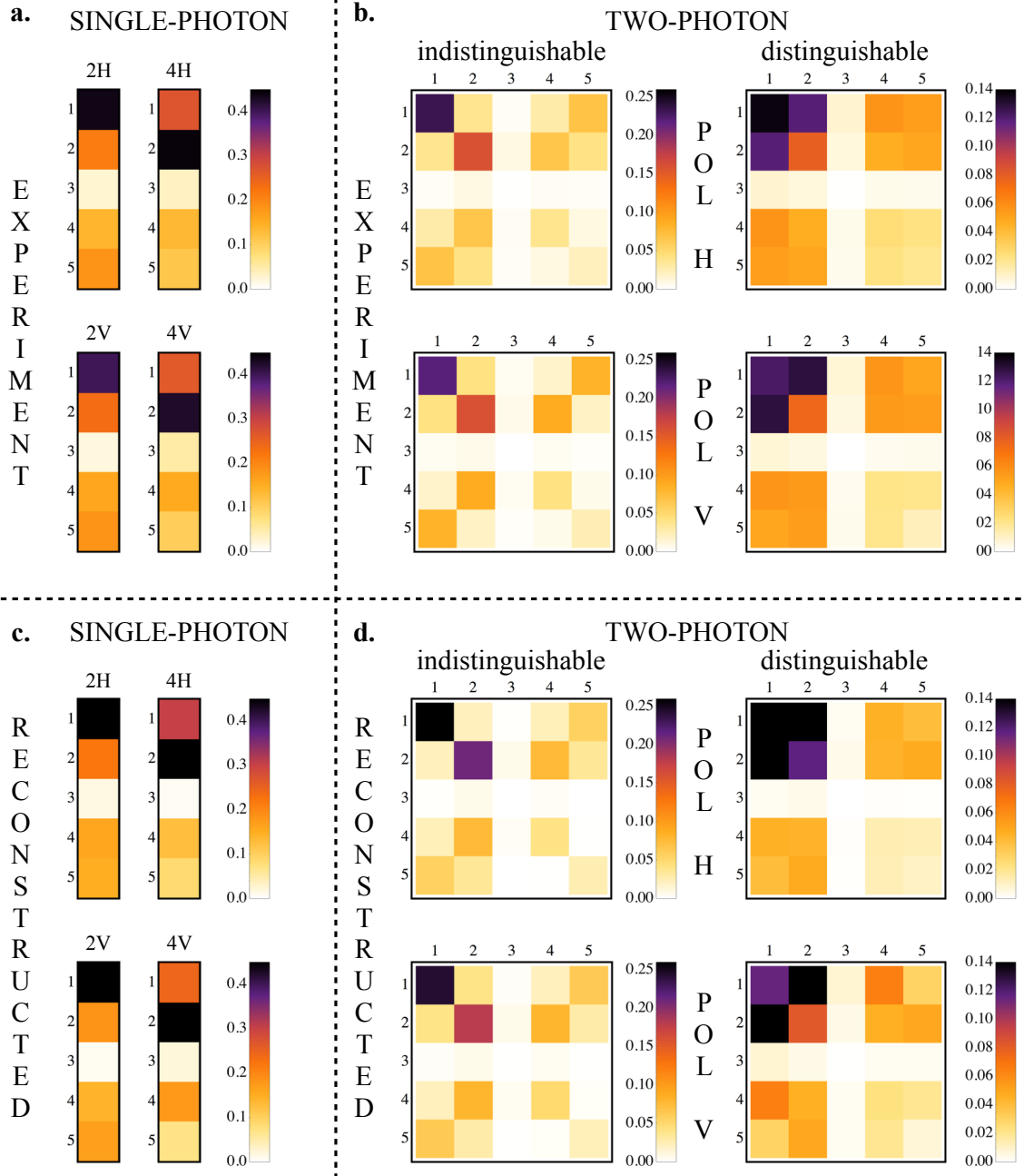


Supplementary Figure 7. Real and imaginary terms for **a-d** theoretical unitary matrix, **b-e** reconstructed unitary matrix for horizontal polarization, and **c-f** reconstructed unitary matrix for vertical polarization.

MODELING THE EVOLUTION WITH THE RECONSTRUCTED UNITARY TRANSFORMATION

Here we briefly discuss how to model the evolution of a polarization entangled state through the quantum transport interferometer. We consider the evolution of an entangled pair through a unitary operator U^π , which in this case presents a small difference for the two orthogonal polarizations. The action of U^π on the field operator before ($a_{j,\pi}^\dagger$) and after ($b_{i,\pi}^\dagger$) the evolution, where $\pi = H, V$ labels the polarization state, is expressed by $a_{j,\pi}^\dagger = \sum_i U_{ji}^\pi b_{i,\pi}^\dagger$. The input state of the process is a two-photon entangled pair in the $|\Psi_{2p}^\pm\rangle_{i,j}$ Bell state, where the photons are injected in input ports i and j :

$$|\Psi_{2p}^\pm\rangle_{i,j} = \frac{1}{\sqrt{2}}(|H\rangle_i|V\rangle_j \pm |V\rangle_i|H\rangle_j) = \frac{1}{\sqrt{2}}(a_{i,H}^\dagger a_{j,V}^\dagger \pm a_{i,V}^\dagger a_{j,H}^\dagger)|0\rangle. \quad (\text{S15})$$



Supplementary Figure 8. **a-b.** Experimental single-photon couplings for input 2 and 4 and two photon unitary transformation, both indistinguishable and distinguishable, for polarization H and V . **c-d.** Numerical prediction from experimentally reconstructed unitary transformation of single-photon probabilities for input 2 and 4 and two-photon interference, both indistinguishable and distinguishable, distribution for polarization H and V . Both single- and two-photon distributions show the polarization insensitivity of the device.

The state after the evolution can be written as:

$$\begin{aligned} |\Psi_{2p}^{\pm}\rangle_{i,j} &\xrightarrow{U_{\mathcal{F}}} \frac{1}{\sqrt{2}} \left[\left(\sum_m U_{i,m}^H b_{m,H}^{\dagger} \right) \left(\sum_n U_{j,n}^V b_{n,V}^{\dagger} \right) \pm \left(\sum_n U_{i,n}^V b_{n,V}^{\dagger} \right) \left(\sum_m U_{j,m}^H b_{m,H}^{\dagger} \right) \right] |0\rangle = \\ &= \frac{1}{\sqrt{2}} \left[\sum_{m,n} (U_{i,m}^H U_{j,n}^V \pm U_{j,m}^H U_{i,n}^V) b_{m,H}^{\dagger} b_{n,V}^{\dagger} \right] |0\rangle. \end{aligned} \quad (\text{S16})$$

The transition amplitudes from input state $|\Psi_{2p}^{\pm}\rangle_{i,j}$ to the output configurations $|rH, sV\rangle$ and $|rV, sH\rangle$ for $r \neq s$ are respectively:

$$\langle rH, sV | U | \Psi_{2p}^{\pm} \rangle_{i,j} = \frac{1}{\sqrt{2}} (U_{i,r}^H U_{j,s}^V \pm U_{j,r}^H U_{i,s}^V) \quad (\text{S17})$$

$$\langle sH, rV | U | \Psi_{2p}^{\pm} \rangle_{i,j} = \frac{1}{\sqrt{2}} (U_{i,s}^H U_{j,r}^V \pm U_{j,s}^H U_{i,r}^V) \quad (\text{S19})$$

where the \pm signs in the transition amplitudes depend on the symmetry of the input entangled state. We can define the submatrices $U_{r,l}^{i,j}$ of U^H and U^V as:

$$U_{r,s}^{i,j} = \begin{pmatrix} U_{i,r}^H & U_{j,r}^H \\ U_{i,s}^V & U_{j,s}^V \end{pmatrix}. \quad (\text{S20})$$

If the input state is in the singlet anti-symmetric state $|\Psi_{2p}^{-}\rangle_{i,j}$, the probability of obtaining a photon on modes r and s can be expressed as:

$$\text{Prob}(r, s | \Psi_{i,j}^{-}) = \frac{1}{2} \left[|\det(U_{r,s}^{i,j})|^2 + |\det(U_{s,r}^{i,j})|^2 \right], \quad (\text{S21})$$

$$\text{Prob}(r, r | \Psi_{i,j}^{-}) = \frac{1}{2} |\det(U_{r,r}^{i,j})|^2 \quad (\text{S23})$$

thus depending on the determinants of the submatrices $U_{r,s}^{i,j}$. Conversely, if the input state is symmetric $|\Psi_{2p}^{+}\rangle_{i,j}$ we obtain:

$$\text{Prob}(r, s | \Psi_{i,j}^{+}) = \frac{1}{2} \left[|\text{per}(U_{r,s}^{i,j})|^2 + |\text{per}(U_{s,r}^{i,j})|^2 \right], \quad (\text{S24})$$

$$\text{Prob}(r, r | \Psi_{i,j}^{+}) = \frac{1}{2} |\text{per}(U_{r,r}^{i,j})|^2 \quad (\text{S26})$$

thus depending on permanents of the submatrices $U_{r,s}^{i,j}$.

CHARACTERISATION OF THE ECC DEVICE

For an ideal fermionic quantum spin transport, the target state would be of the form $|\psi_{\text{ideal}}\rangle = |\psi_{1p}^{+}\rangle_{24} |\psi_{1p}^{+}\rangle_{15} |0\rangle_3$. Our device is a finite engineered chain and the generated state is $|\psi_{\text{out}}\rangle = (\alpha|10\rangle_{15} + \beta|01\rangle_{15})(\gamma|10\rangle_{24} + \delta|01\rangle_{24})|0\rangle_3$, where the terms α , β , γ and δ define an unbalancement due to the approximation of the perfect state.

The coherence between the path entangled states is studied using the second device, comprised of integrated beam splitters and thermal phase shifters. In particular, with suitable phases before

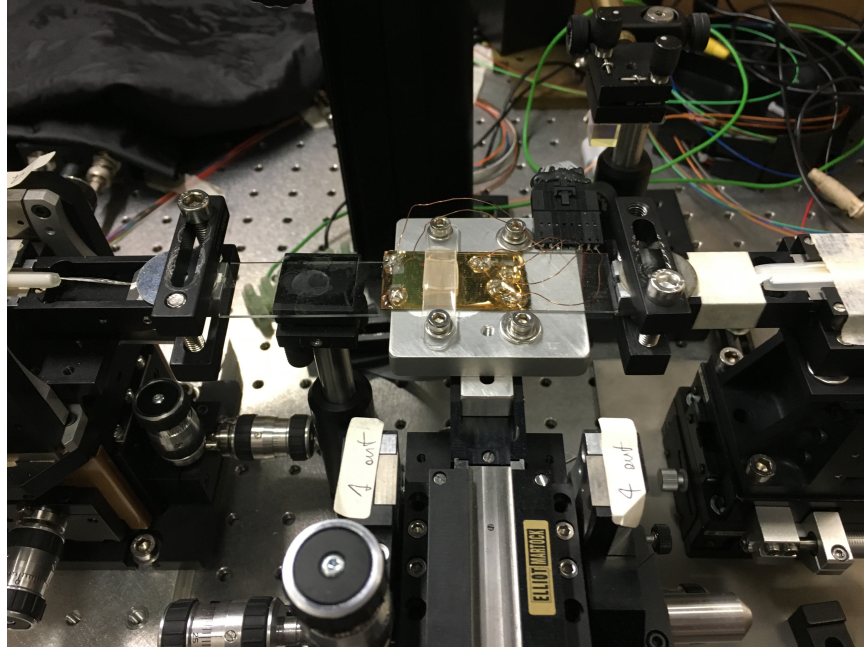
the two beam-splitters, the target state would result in a photon in output mode 2 and a photon in output mode 5. The phase χ of the liquid crystal for the injection of a singlet $|\Psi_{2p}^-\rangle$ state is set by measuring the physical quantity $(P'_{12} + P'_{14} + P'_{25} + P'_{45}) - (P'_{24} + P'_{15})$ at the output of the second device, where P'_{ij} is the coincidence probability at modes i and j . Such quantity is maximized for input state $|\Psi_{2p}^-\rangle$ and minimized for input state $|\Psi_{2p}^+\rangle$.

The phase shifters in the second device are actively controlled via thermal resistors. Each thermal resistor is connected to an external power supply with independent voltage channel control and the applied voltage ranges between 0 V to 7 V, in which a full 2π oscillation period is seen. Overall transmission efficiency from delay lines to the photodetectors is approximately 0.6%, which includes transmission losses inside the two chips and coupling losses at the four interfaces between delay line, input fiber array, first chip, second chip and output fiber array. Coincidence rates for all outputs are measured by singularly tuning the applied phase shift from each thermal resistors, showing a 2π oscillation within ~ 0.8 W dissipated power. When evaluating the expected curves for the quantities S_1 and S_5 as a function of ϕ_5 , losses corresponding to an additional efficiency $\eta_5 = 0.36$ is considered for mode 5 at the interface between the two devices. This quantity is retrieved from characterisation with classical light. Each experimental distribution is compared to its theoretical prediction though the measurement of the similarity, which is defined in terms of all contributions of the correlation function

$$\mathcal{S}^{B(F)} = \frac{\left(\sum_{ij} \sqrt{\Gamma_{ij}^{B(F)} \tilde{\Gamma}_{ij}^{B(F)}} \right)^2}{\left(\sum_{ij} \Gamma_{ij}^{B(F)} \sum_{ij} \tilde{\Gamma}_{ij}^{B(F)} \right)}. \quad (\text{S27})$$

where the $\tilde{\Gamma}_{ij}$ and Γ_{ij} are experimental and theoretical correlation function for mode i and j for bosons (B) and fermions (F).

-
- [S1] Strauch, F. W. Connecting the discrete- and continuous-time quantum walks *Phys. Rev. A* **74** 030301 (2006).
 - [S2] Kurzyński, P. & Wójcik A. Discrete-time quantum walk approach to state transfer *Phys. Rev. A* **83** 062315 (2011).
 - [S3] Christandl, M., Datta, N., Ekert, A. & Landahl A. J. Perfect state transfer in quantum spin networks *Phys. Rev. Lett.* **92** 187902 (2004).
 - [S4] Banchi, L., Apollaro, T., Cuccoli, A., Vaia, R. & Verrucchi, P. Long quantum channels for high-quality entanglement transfer *New J. Phys.* **13** 123006 (2011).
 - [S5] Alkurtass, B., Banchi, L. & Bose, S. Optimal quench for distance-independent entanglement and maximal block entropy *Phys. Rev. A* **60** 042304 (2014).
 - [S6] Hong, C. K., Ou, Z. Y. & Mandel, L. Measurement of subpicosecond time intervals between two photon by interference. *Phys. Rev. Lett.* **59** 2044-2046 (1987).
 - [S7] Laing, A. & O'Brien, J. L. Super-stable tomography of any linear optical device Preprint arXiv:1208.2868v1[quant-ph] (2012).
 - [S8] Crespi, A. *et. al.*. Suppression law of quantum states in a 3D photonic fast Fourier transform chip. *Nature Commun.* **7** 10469 (2015)



Supplementary Figure 9. Photograph of the experimental setup. From the left: input single-mode fiber array, chip with quantum transport device, chip with thermal resistor and entanglement check device, output multi-mode fiber array.